Molecular Catalysis 484 (2020) 110731

Contents lists available at ScienceDirect

Molecular Catalysis

journal homepage: www.elsevier.com/locate/mcat

Dimethyl oxalate synthesis via CO oxidation on Pd-doped Ag(111) surface: A theoretic study

Bingying Han[a], Lixia Ling[b,c,d,*], Riguang Zhang[a], Ping Liu[c], Maohong Fan[d], Baojun Wang[a,*]

[a] Key Laboratory of Coal Science and Technology of Ministry of Education and Shanxi Province, Taiyuan University of Technology, Taiyuan 030024, PR China
[b] College of Chemistry and Chemical Engineering, Taiyuan University of Technology, Taiyuan 030024, PR China
[c] State Key Laboratory of Coal Conversion, Institute of Coal Chemistry, Chinese Academy of Sciences, Taiyuan 030001, PR China
[d] Department of Chemical and Petroleum Engineering, University of Wyoming, 1000 E University Ave, Laramie, WY 82071, USA

ARTICLE INFO

Keywords:
Pd_{ML}/Ag(111)
Pd_4Ag_8/Ag(111)
Pd_1-Ag(111)
CO oxidation to dimethyl oxalate
DFT combined with micro-kinetic analysis

ABSTRACT

High-efficiency and low-cost Pd-based catalyst is of vital importance toward CO oxidation to dimethyl oxalate (DMO). Here, we design Pd monolayer, Pd stripe and Pd single atom embedded on Ag(111) surfaces, i.e. Pd_{ML}/Ag(111), Pd_4Ag_8/Ag(111) and Pd_1-Ag(111), to investigate the effect of different content of Pd atoms in Ag substrate toward DMO formation. The density functional theory (DFT) calculation illustrates that the optimal pathway to produce DMO is two $COOCH_3$ intermediates coupling route on three catalyst surfaces, which is the same to the Pd(111) surface, showing that it has no influence on the favorable route of DMO formation. Additionally, the DFT combined with micro-kinetic analysis indicates that Pd_1-Ag(111) exhibits the highest activity for DMO generation, Pd_{ML}/Ag(111) is superior to Pd(111), while Pd_4Ag_8/Ag(111) is inferior to Pd(111). Among them, the high activity on the Pd_1-Ag(111) is attributed to strain effect and ligand effect both reducing activation barrier of the rate-controlling step. Moreover, Pd_1-Ag(111) shows high selectivity for DMO, whereas it is opposite on the Pd_{ML}/Ag(111). Therefore, it is proposed that Pd_1-Ag single atom surface alloy can be the promising candidate not only improving the noble Pd's catalytic performance for DMO formation but also reducing its usage.

1. Introduction

Dimethyl oxalate (DMO) is one of the most important chemicals produced worldwide, and an essential raw material in the highly efficient production of ethylene glycol (EG) [1–3]. In past decades, DMO was mainly produced by oxidative carbonylation of methanol, carbon monoxide and oxygen under $PdCl_2$-$CuCl_2$ catalysts, however the entire reaction was proceeding in the liquid phase, which led to many disadvantages such as catalyst deactivation, equipment corrosion and so on [4]. In order to solve these problems caused by liquid phase, the gas phase coupling method to produce DMO has been developed via introducing methyl nitrite (CH_3ONO, MN) as a key agent in recent years and getting more and more attention, where the introduced CH_3ONO is a well-known unstable substance and susceptible to be dissociated to generate OCH_3 and NO [5,6]. Among them, the OCH_3 groups can be catalyzed with Pd-based catalysts to generate DMO [7,8], and the NO is easily desorbed to proceed non-catalytic regeneration of CH_3ONO [9,10], which can be expressed by the equations, respectively: $2CO + 2CH_3O \rightarrow (COOCH_3)_2$ and $2CH_3OH + 2NO + 1/2O_2 \rightarrow 2CH_3ONO + H_2O$. The entire reaction process of DMO formation via gas phase method is environmentally friendly and highly efficient.

Pd has been demonstrated to be the sole metal that exhibits remarkable catalytic performance for gas-phase method to synthesize DMO, whose (111) plane has been also identified to be the master active surface [11]. However, the large-scale industrial application of gas-phase method is hindered owing to high Pd amount in the industrial catalyst and expensive Pd cost [12]. In view of this, it is imperative to lessen Pd usage in the precondition of its outstanding catalytic performance. As well known, the relatively cheaper metals have been widely used as the substrates to synthesize bimetallic catalysts with low Pd dosage and extraordinary catalytic performance [13–16].

More recently, the study of experiment shows that Ag can be as the fine carrier, of which price is lower than that of Pd, and surface Ag atoms can be selectively etched to offer sites for Pd deposition [17]. Wang et al. [18] prepared Pd/CNTs and Pd-on-Ag/CNTs through the atomic layer deposition (ALD) approach for the reaction of formic acid oxidation and found the catalytic activity of Pd-on-Ag/CNTs was higher than that of Pd/CNTs. The electron interaction between the Ag carrier

* Corresponding authors at: No. 79 West Yingze Street, Taiyuan University of Technology, Taiyuan 030024, PR China.
E-mail addresses: linglixia@tyut.edu.cn (L. Ling), wangbaojun@tyut.edu.cn (B. Wang).

https://doi.org/10.1016/j.mcat.2019.110731
Received 21 August 2019; Received in revised form 22 November 2019; Accepted 27 November 2019
Available online 19 December 2019
2468-8231/ © 2019 Elsevier B.V. All rights reserved.

and the Pd active component reduced the adsorption energy of CO over Pd-on-Ag/CNTs, thereby enhancing its anti-deactivation performance. The selective hydrogen production by formic acid dissociation on Pd/Ag(111) has been studied by DFT calculation, and it was found that the layer numbers of the supported Pd was different, and the selectivity toward hydrogen production was also different. When the Pd layer number on Pd/Ag(111) was the monolayer, the binding degree of key intermediates (HCO and HCOO) to the surface was reduced, thereby enhancing the selectivity of hydrogen formation [19]. And, Pd/Ag interface alloy has been experimentally prepared by Pd deposition on the Ag(111) surface [20–23]. Besides, Tedsree et al. [24] synthesized a bimetallic catalyst with a thin layer of Pd supported on Ag nanoparticles by liquid phase reduction method. The result of atomic probe tomography showed that the bimetallic nanoparticles possessed a well core-shell structure. The activity toward the dissociation of formic acid on Ag@Pd was much higher than that on pure Pd, which was due to the electron action between Ag carrier and Pd. Besides, the Ag(111) surface doped with a trace amount of Pd atoms in the surface layer has been studied toward CO oxidation reaction by DFT calculation, which was further compared with Ag(111) and Pd(111) surfaces. It was found that the energy barrier of CO oxidation reaction was the lowest on the Pd-Ag/Ag (111) surface. This was because the adsorption of CO on the Pd-Ag/Ag(111) surface was weak chemical adsorption and easy to be activated; while it was physical adsorption on the Ag (111) surface, which was easy to be desorbed; and it was strong chemical adsorption on Pd (111) and difficult to be activated [25]. Additionally, Li et al. [17] prepared Ag@PdAg catalyst by inserting a small amount of Pd atoms into Ag nanoparticles by selective deposition etching method. The core-shell structure could facilitate the electron resolve of the adsorbed H atoms, thus promoting hydrogen evolution reaction. Its catalytic activity was 14 times that of conventional Pd catalysts. The strategy of embedding the noble metal Pd in the Ag carrier improves the catalytic performance and reduces the catalyst cost. And, Ag@PdAg catalyst has been demonstrated that possessed much higher catalytic performance than PdAg alloy and pure Pd catalysts [26]. Reducing the amount of Pd atoms to the limit, that is, isolated Pd atoms are doped in Ag substrate to form Pd_1-Ag single atom surface alloy. Aich et al. [27] adopted a wet impregnation method to ember a small amount of Pd atoms into the Ag carrier, the analysis result by EXAFS showed that Pd had been individually dispersed in the Ag nanoparticles forming the Pd_1-Ag single atom surface alloy, when the concentration of doped Pd atoms was below 0.01 wt%. Compared with the pure Pd, Pd_1-Ag single atom alloy exhibited higher activity of acrolein hydrogenation.

As mentioned above, Pd/Ag, Pd-Ag/Ag and Pd_1-Ag bimetallic catalysts showed outstanding catalytic performance toward specific chemical reactions [17–19,24–27]. However, there has been no related research about synthesis of DMO from CO oxidation on these catalysts. Nowadays, computation-designing high performance catalysts has been increasingly receiving recognition and attention [13,28–32]. Thus, in this study, the DFT method united with micro-kinetic analysis is employed to research DMO synthesis via CO oxidation on Pd monolayer, Pd stripe and Pd single atom embedded in Ag(111) which represent different content of Pd atoms in Ag substrate, in order to obtain a low Pd content but excellent catalytic performance of Pd-Ag bimetallic catalysts.

It is known that the extraordinary catalytic performance of bimetallic catalysts can be ascribed to the united strain effect and ligand effect, in which strain effect arises from the tension or compression of stress induced by carrier metal to doped metal as well as ligand effect refers to charge change of doped metal caused by substrate metal [33–37]. And, the DFT calculation has been used to investigate the effects of strain and ligand on formic acid dissociation to hydrogen over the Pd/Ag(111) surface, and it was found that the ligand effect caused by electron transfer between Ag carrier and Pd had main influence on selective hydrogen production by formic acid dissociation, and strain effect resulted from different lattice constants of Ag and Pd had less impact on it [19]. However, it is still unclear that how strain and ligand effect impact DMO synthesis over Pd monolayer, Pd stripe and Pd single atom embedded on Ag(111), which remains to be clarified.

2. Methods and models

All the DFT calculations presented in this work were executed with Vienna Ab-initio Software Package (VASP) [38,39] utilizing exchange-correlation functional of GGA-PBE [40]. The interaction of electron-ion has been depicted by Projector-augmented wave (PAW) approach [41,42]. The k-point mesh being (3 × 2 × 1) and cutoff energy of 400 eV were employed to sample Brillouin zone and expand plane wave basis, respectively. Self-successive iteration was thought to be converged for the optimization of geometry structure when force change and energy difference were below 0.03 eV·Å^{-1} and 1 × 10^{-5} eV, respectively. Additionally, the transition state (TS) was obtained by adopting the CI-NEB (climbing-image nudged elastic band) [43,44] combined with dimer approach [45,46] till the force difference was below 0.05 eV·Å^{-1}, and further identified by confirming that there existed a sole imaginary frequency on the reaction coordinate.

The zero-point energy (ZPE) is considered to correct the electronic energy, and determined by

$$\mathrm{ZPE} = \sum_{i=1} \frac{h\nu_i}{2} \tag{1}$$

where h stands for Planck constant, and ν_i reprensts real frequency. Additionally, activation energy of E_a and reaction energy of ΔE are calculated as

$$E_a = E_{TS} - E_{IS} \tag{2}$$

and

$$\Delta E = E_{FS} - E_{IS} \tag{3}$$

where E_{IS} denotes the energy of initial state, E_{TS} means that of transition state, and E_{FS} represents that of final state. The rate constant of each step can be obtained by the harmonic transition state theory (TST) [47]:

$$k = \frac{k_B T}{h} \frac{\prod_{i=1}^{3N} [1 - \exp(-\frac{h\nu_i^{IS}}{k_B T})]}{\prod_{i=1}^{3N-1} [1 - \exp(-\frac{h\nu_i^{TS}}{k_B T})]} \exp\left(\frac{-E_a}{RT}\right) \tag{4}$$

as presented in Table 2, where k_B is on behalf of Boltzmann constant, and T refers to temperature, as well as ν_i^{IS} represents real frequencies of initial state and ν_i^{TS} is that of transition state.

The calculated lattice parameters of Pd and Ag are 3.955 and 4.153 Å, and constant with the experimental ones (Pd, 3.900 [48]; Ag, 4.086 Å [49]). The pure Ag(111) surface is firstly modeled via constructing a three layers of 3 × 4 × 1 supercell. Then, Pd monolayer, Pd stripe and Pd single atom-embedded Ag(111) are built by displacing monolayer Ag atoms, four striped Ag atoms and single Ag atom with Pd atoms on surface layer of Ag(111), i.e. Pd_{ML}/Ag(111), Pd_4Ag_8/Ag(111) and Pd_1-Ag(111). The same method has been used to construct Pd_{ML}/Cu(111), Pd_4Cu_8/Cu(111) and Pd_1-Cu(111) to represent Cu substrate doped by Pd monolayer, Pd stripe and Pd single atom [7,50]. And, the bottom one layer is kept frozen while the other layers with adsorbates are approved to completely relax (Fig. 1).

Additionally, the vacuum layer of 10 Å is set so as to prevent the periodic interaction of repeated slabs. Here, the vacuum layer refers to the region added to the surface of catalyst slab model, and its thickness is from the surface of the slab model to the bottom of another periodic slab model in the vertical direction. Moreover, to verify the selected vacuum thickness of 10 Å is sufficient for the calculated system, the activation barrier and reaction energy of the first elementary step ($CO + OCH_3 \rightarrow COOCH_3$) on Pd_{ML}/Ag(111) at the vacuum thickness of 15 Å are calculated, and compared with that at the vacuum thickness of 10 Å. The results indicate that the corresponding activation barrier and

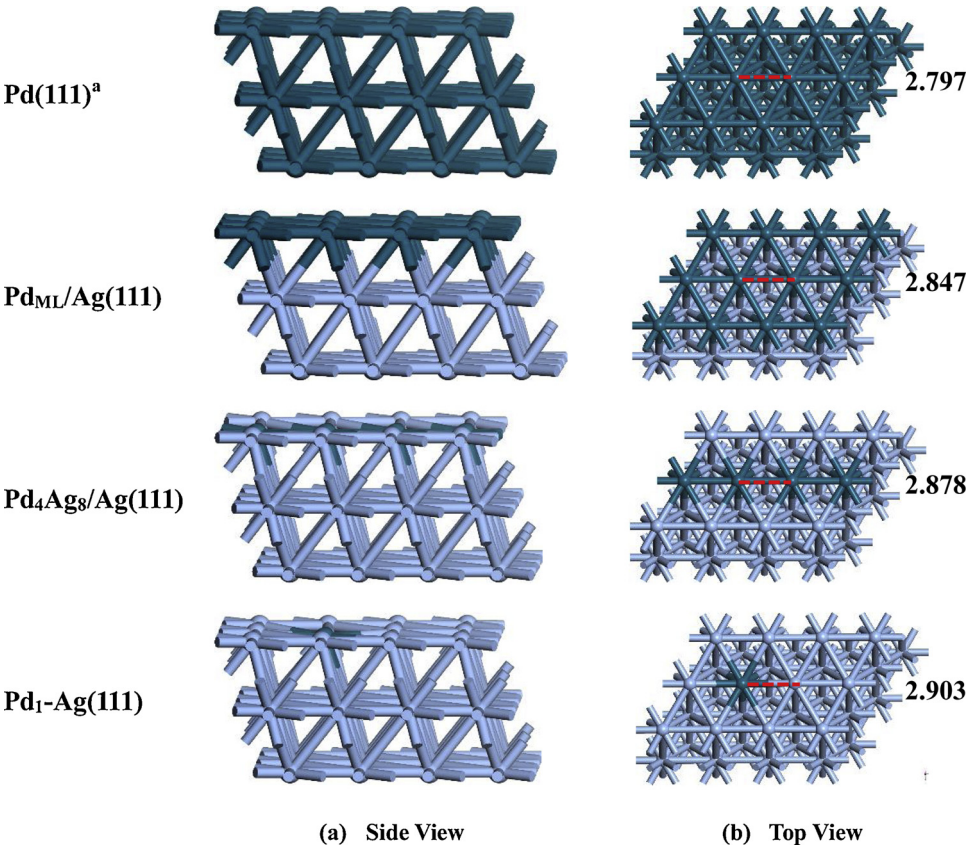

Fig. 1. The surface morphologies of Pd_{ML}/Ag(111), Pd_4Ag_8/Ag(111) and Pd_1-Ag(111) surfaces. Dark cyan and silver white balls denote Pd and Ag, respectively. [a] The previous study [50].

reaction energy are 28.9 and -63.5 kJ/mol at the vacuum thickness of 15 Å, which is very consistent with 26.4 and -63.1 kJ/mol at the vacuum thickness of 10 Å, implying that there exists little influence on activation barrier and reaction energy with the vacuum thickness increases.

To demonstrate the sufficiency of the selected cutoff energy (400 eV), the activation barrier and reaction energy of three elementary steps in the $COOCH_3$-$COOCH_3$ coupling path on the Pd_{ML}/Ag(111) surface at the cutoff energy of 550 eV are calculated, and further compared with those at the cutoff energy of 400 eV, respectively. The results show that the activation barrier and reaction energy of each elementary step are 27.8 and -63.1 kJ/mol, 93.9 and 40.7 kJ/mol, 118.8 and -2.4 kJ/mol at the cutoff energy of 550 eV, respectively, which are very close to the values of 26.4 and -63.1 kJ/mol, 96.0 and 41.3 kJ/mol, 116.7 and -3.6 kJ/mol obtained at the cutoff energy of 400 eV, respectively, intimating that the activation barrier and reaction energy do not change very much when the cutoff energy increases from 400 to 550 eV. Therefore, taking account the calculation efficiency, the selected cutoff energy (400 eV) is considered to be sufficient and suitable for the calculated systems.

And, the influence of dipole correction on the energy barrier and reaction energy of the first elementary step ($CO + OCH_3 \rightarrow COOCH_3$) on Pd_{ML}/Ag(111), Pd_4Ag_8/Ag(111) and Pd_1-Ag(111) has been studied. The results show that the corresponding energy barrier and reaction energy are 27.2 and -66.0 kJ/mol on Pd_{ML}/Ag(111), 35.0 and -18.5 kJ/mol on Pd_4Ag_8/Ag(111), 1.8 and -44.1 kJ/mol on Pd_1-Ag(111), which are very close to the values of 26.4 and -63.1, 34.2 and -20.3, 0.6 and -44.3 kJ/mol obtained without dipole correction, respectively, indicating that there exists little difference for the results when the dipole correction is added into system. Thus, dipole correction is ignored in the work. The same treatment approach has been adopted in previous study due to little impact of the dipole correction [7,51,52].

3. Results and discussion

3.1. Catalytic activities of DMO production on Pd_{ML}/Ag(111), Pd_4Ag_8/Ag(111) and Pd_1-Ag(111)

The initial reactant of CH_3ONO is a well-known unsteady substance and easily inclined to be decomposed to produce OCH_3 radical [5,6], thence DMO generation can be thought to start with OCH_3 radical in the following study. According to different types of C—C bond coupling, the pathways of DMO formation can be divided into three, as presented in Scheme 1. However, the results indicate that OCCO intermediate formed by the coupling of two CO in Path3 is very unsteady over these catalyst surfaces and readily breaks down into two CO. The calculated energy barrier E_a and reaction energy ΔE that are related with the process of CO oxidation to DMO on Pd_{ML}/Ag(111), Pd_4Ag_8/Ag(111) and Pd_1-Ag(111), have been listed in Table 1.

In addition, to demonstrate whether pure Ag substrate can catalyze this reaction or not, the Ag(111) surface has been studied for DMO synthesis. The preliminary steps ($CO + OCH_3 \rightarrow COOCH_3$, $CO + CO \rightarrow OCCO$) are firstly studied. The reaction of DMO synthesis is thought not to happen when the preliminary step cannot be proceeded. The results

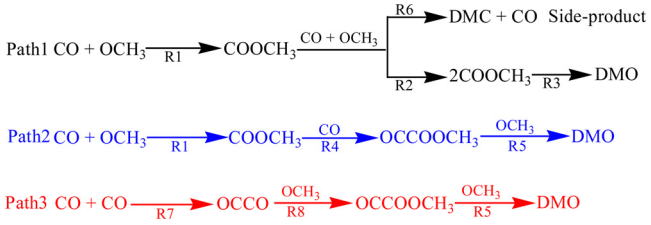

Scheme 1. Proposed reaction paths [8] for DMO synthesis via CO oxidation.

Table 1
The obtained energy barrier E_a and reaction energy ΔE (kJ·mol^{-1}) related with the process of CO oxidation to DMO on Pd_{ML}/Ag(111), Pd_4Ag_8/Ag(111) and Pd_1-Ag(111).

Surface	Elementary reactions	E_a	ΔE
Pd_{ML}/Ag(111)	$CO + OCH_3 \rightarrow COOCH_3$	26.4	−63.1
	$COOCH_3 + CO + OCH_3 \rightarrow 2COOCH_3$	96.0	41.3
	$2COOCH_3 \rightarrow (COOCH_3)_2$	116.7	−3.6
	$COOCH_3 + CO \rightarrow OCCOOCH_3$	135.1	96.9
	$OCCOOCH_3 + OCH_3 \rightarrow (COOCH_3)_2$	33.4	−95.2
	$COOCH_3 + CO + OCH_3 \rightarrow DMC + CO$	59.5	−107.8
Pd_4Ag_8/Ag(111)	$CO + OCH_3 \rightarrow COOCH_3$	34.2	−20.3
	$COOCH_3 + CO + OCH_3 \rightarrow 2COOCH_3$	31.6	−30.4
	$2COOCH_3 \rightarrow (COOCH_3)_2$	122.6	0.7
	$COOCH_3 + CO \rightarrow OCCOOCH_3$	156.6	96.1
	$OCCOOCH_3 + OCH_3 \rightarrow (COOCH_3)_2$	30.9	−92.0
	$COOCH_3 + CO + OCH_3 \rightarrow DMC + CO$	266.3	11.1
Pd_1-Ag(111)	$CO + OCH_3 \rightarrow COOCH_3$	0.6	−44.3
	$COOCH_3 + CO + OCH_3 \rightarrow 2COOCH_3$	42.7	−11.8
	$2COOCH_3 \rightarrow (COOCH_3)_2$	54.6	−57.7
	$COOCH_3 + CO \rightarrow OCCOOCH_3$	93.8	5.6
	$OCCOOCH_3 + OCH_3 \rightarrow (COOCH_3)_2$	31.0	−74.3
	$COOCH_3 + CO + OCH_3 \rightarrow DMC + CO$	97.5	−34.1
Pd(111)[a]	$CO + OCH_3 \rightarrow COOCH_3$	38.1	−25.6
	$COOCH_3 + CO + OCH_3 \rightarrow 2COOCH_3$	52.5	−17.5
	$2COOCH_3 \rightarrow (COOCH_3)_2$	120.6	53.6
	$COOCH_3 + CO \rightarrow OCCOOCH_3$	160.1	117.0
	$OCCOOCH_3 + OCH_3 \rightarrow (COOCH_3)_2$	31.2	−43.2
	$COOCH_3 + CO + OCH_3 \rightarrow DMC + CO$	153.5	−110.8

[a] The previous study [50].

show that when the structure of transition state is searched for $CO + OCH_3 \rightarrow COOCH_3$, it appears to be severely deformed and deviates from the lowest energy route, resulting in that the structure of transition state cannot be obtained, which implies that the step does not happen. For example, the structures of transition states for CH hydrogenation to CH_2 cannot be obtained on Cu_{38} and Cu_{55} clusters, which indicates that the reaction of CH to CH_2 does not take place [53]. Additionally, the preliminary step of $CO + CO \rightarrow OCCO$ does not also occur, which is because OCCO intermediate is readily resolved to two CO over the Ag(111) surface. Therefore, it can be obtained that DMO synthesis does not happen over the pure Ag(111) surface.

3.1.1. Catalytic activity of DMO production on the Pd_{ML}/Ag(111)

On the Pd_{ML}/Ag(111), Path1 originates from co-adsorption of OCH_3 and CO, in which OCH_3 and CO occupy on two neighbor top sites and the corresponding energy of co-adsorption is -214.7 kJ·mol^{-1}, seen in Fig. 2. Hereafter, OCH_3 assaults CO to produce the key intermediate of $COOCH_3$ through the transition state TS1, and the energy barrier is 26.4 kJ·mol^{-1} with reaction energy being -63.1 kJ·mol^{-1}, as well as the distance of C1···O2 is shortened from 3.575 to 2.186 Å in TS1. The generated $COOCH_3$ intermediate binds to Pd top site, then the other CO and OCH_3 are adsorbed at two adjacent fcc sites, respectively. The second $COOCH_3$ can be subsequently generated through the adsorbed OCH_3 attacking CO, accordingly bringing about the formation of $COOCH_3$-$COOCH_3$ intermediate, and activation barrier is 96.0 kJ·mol^{-1} via TS2 together with endergonic energy being 41.3 kJ·mol^{-1}, as well as the distance of C3···O4 is shrunk to 1.996 in TS2 from 3.160 Å. Finally, the formed $COOCH_3$-$COOCH_3$ is self-coupled to generate the target product DMO by TS3, and corresponding activation energy is 116.7 kJ·mol^{-1} with the reaction heat being -3.6 kJ·mol^{-1}. This step is thought to be the rate-controlling step in Path1, and its activation energy is below those (120.6 and 132.2 kJ·mol^{-1}) on Pd(111) and Pd_{ML}/Cu(111) [50]. Therefrom, for the catalytic activity in Path1 to produce DMO, Pd_{ML}/Ag(111) is stronger than Pd(111) and Pd_{ML}/Cu(111).

With regard to Path2, based on generated $COOCH_3$ intermediate in the first step, the other CO is adsorbed at bridge site, afterwards $COOCH_3$ approaches CO to generate $OCCOOCH_3$ intermediate through TS4, and the reaction heat is 96.9 kJ·mol^{-1} with the activation barrier being 135.1 kJ·mol^{-1}. Lastly, OCH_3 binds to the bridge site and approaches the $OCCOOCH_3$ intermediate to produce final product DMO by TS5, and the corresponding activation and reaction energy are 33.4 and -95.2 kJ·mol^{-1}, respectively. It can be obtained that the second step of $COOCH_3 + CO \rightarrow OCCOOCH_3$ is speed-determining in Path 2, and its energy barrier is rather bigger compared to that of Path1 (135.1 VS 116.7 kJ·mol^{-1}), thereupon Path1 is the favorable route on the Pd_{ML}/Ag(111).

3.1.2. Catalytic activity of Pd_4Ag_8/Ag(111) toward DMO formation

Inspired by the previous work that Cu substrate doped by Pd stripe or Pd single atom could improve the catalytic performance for DMO formation [7], Ag substrate doped by Pd stripe or Pd single atom is constructed in the work and studied for CO oxidation to DMO, observing whether the selectivity can be improved with the further reduction of Pd amount. On the Pd_4Ag_8/Ag(111) surface, for the first step of $CO + OCH_3 \rightarrow COOCH_3$ in Path1, the initial reactant of OCH_3 and CO adsorb at Ag-Pd-Ag fcc and Pd top sites, subsequently OCH_3 is activated to assault CO forming the $COOCH_3$ intermediate through TS1, as shown in Fig. 3, and it needs an energy barrier being 20.3 kJ·mol^{-1} and is exothermic by 34.2 kJ·mol^{-1}. In addition, the distance of C1···O2 is diminished from 3.577 to 2.066 Å in TS1. Starting with the co-adsorption of $COOCH_3$, CO and OCH_3, the second $COOCH_3$ is generated via TS2, bringing about the generation of $COOCH_3$-$COOCH_3$, which has

Table 2
The rate constant (k, s^{-1}) for each step.

		375 K	385 K	395 K	405 K	415 K
Pd_{ML}/Ag(111)	k_1	2.21×10^{8}	2.77×10^{8}	3.43×10^{8}	4.20×10^{8}	5.10×10^{8}
	k_2	5.95×10^{-1}	1.35×10^{0}	2.93×10^{0}	6.12×10^{0}	1.24×10^{1}
	k_3	5.50×10^{-5}	1.47×10^{-4}	3.72×10^{-4}	9.01×10^{-4}	2.09×10^{-3}
	k_4	1.02×10^{-6}	3.18×10^{-6}	9.32×10^{-6}	2.59×10^{-5}	6.87×10^{-5}
	k_5	7.60×10^{8}	1.02×10^{9}	1.34×10^{9}	1.74×10^{9}	2.24×10^{9}
	k_6	8.71×10^{3}	1.44×10^{4}	2.33×10^{4}	3.68×10^{4}	5.69×10^{4}
Pd_4Ag_8/Ag(111)	k_1	7.49×10^{6}	9.94×10^{6}	1.30×10^{7}	1.68×10^{7}	2.14×10^{7}
	k_2	1.20×10^{8}	1.56×10^{8}	2.01×10^{8}	2.55×10^{8}	3.20×10^{8}
	k_3	6.50×10^{-7}	1.74×10^{-6}	4.43×10^{-6}	1.08×10^{-5}	2.50×10^{-5}
	k_4	1.45×10^{-9}	5.42×10^{-9}	1.90×10^{-8}	6.25×10^{-8}	1.94×10^{-7}
	k_5	1.45×10^{8}	1.88×10^{8}	2.42×10^{8}	3.06×10^{8}	3.83×10^{8}
	k_6	6.65×10^{-23}	6.36×10^{-22}	5.43×10^{-21}	4.17×10^{-20}	2.90×10^{-19}
Pd_1-Ag(111)	k_1	7.04×10^{12}	7.14×10^{12}	7.24×10^{12}	7.33×10^{12}	7.42×10^{12}
	k_2	1.71×10^{5}	2.44×10^{5}	3.41×10^{5}	4.69×10^{5}	6.36×10^{5}
	k_3	2.83×10^{5}	4.51×10^{5}	7.01×10^{5}	1.07×10^{6}	1.59×10^{6}
	k_4	2.70×10^{0}	5.98×10^{0}	1.28×10^{1}	2.62×10^{1}	5.19×10^{1}
	k_5	2.61×10^{6}	3.35×10^{6}	4.25×10^{6}	5.32×10^{6}	6.60×10^{6}
	k_6	2.44×10^{-1}	5.61×10^{-1}	1.23×10^{0}	2.61×10^{0}	5.33×10^{0}

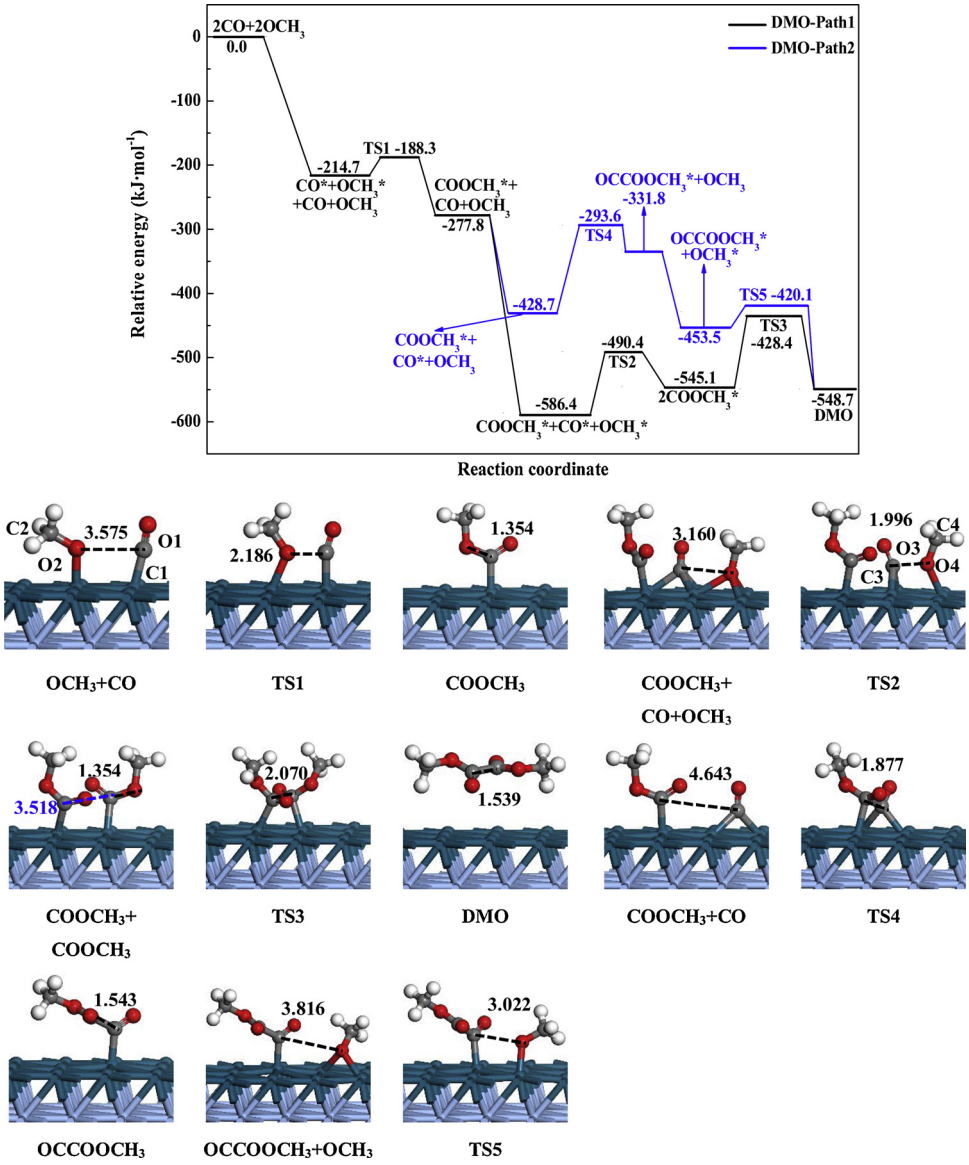

Fig. 2. The energy diagram toward DMO formation with corresponding configurations on the Pd_{ML}/Ag(111).

the barrier being 31.6 kJ·mol^{-1} and reaction energy of -30.4 kJ·mol^{-1}. Ultimately, the product DMO can be synthesized via the self-coupling of $COOCH_3$-$COOCH_3$ intermediate, and barrier energy is 122.6 kJ·mol^{-1} via TS3 with reaction energy being 0.7 kJ·mol^{-1}.

In terms of Path2, the generated $COOCH_3$ in the first step connects with CO to generate $OCCOOCH_3$ intermediate by TS4 with the reaction energy of 96.1 kJ·mol^{-1} and barrier being 156.6 kJ·mol^{-1}. The distance of C1···C3 is shortened to 1.904 Å in TS4 from 4.573 Å. Finally, $OCCOOCH_3$ attacks OCH_3 to form DMO via TS5 together with the reaction energy of -92.0 kJ·mol^{-1} and activation energy of 30.9 kJ·mol^{-1}. In summary, the rate-controlling steps in Path1 and Path2 are R3 and R4 with the activation energy being 122.6 and 156.6 kJ·mol^{-1}, respectively, implying Path1 is the advantageous route to form DMO.

3.1.3. Catalytic activity for DMO production on the Pd_1-Ag(111)

Based on the study of DMO generation over Pd_{ML}/Ag(111) and Pd_4Ag_8/Ag(111), minimizing the usage of Pd noble metal to the limit, Pd single atom-embedded on the Ag(111), i.e. Pd_1-Ag(111), is constructed and investigated toward CO oxidation to DMO. As presented in Fig. 4, OCH_3 and CO firstly bind to Ag-Pd-Ag hcp and Pd-Ag bridge sites together with the exothermic energy of 228.7 kJ·mol^{-1}, then OCH_3 assaults CO to generate $COOCH_3$ intermediate by TS1 with distance of C1···O2 being 2.129 Å, which is with the activation energy of 0.6 kJ·mol^{-1} and exothermic heat of 44.3 kJ·mol^{-1}. Subsequently, the $COOCH_3$-$COOCH_3$ intermediate can be formed with the other $COOCH_3$ generation by TS2, and the barrier energy of 42.7 kJ·mol^{-1} and exothermic energy of 11.8 kJ·mol^{-1} are wanted in this step. Finally, DMO is generated via the $COOCH_3$-$COOCH_3$ intermediate self-coupling, and the relevant barrier energy is 54.6 kJ·mol^{-1} though TS3 with the reaction energy of -57.7 kJ·mol^{-1}.

With respect to Path2, the $OCCOOCH_3$ intermediate is generated through $COOCH_3$ attacking CO with the TS4 with the activation and reaction heat of 93.8 and 5.6 kJ·mol^{-1}, where distance of C1···C3 in TS4 is 1.991 Å. Then, $OCCOOCH_3$ connects with OCH_3 to produce DMO via TS5, and the reaction heat is -74.3 kJ·mol^{-1} with activation barrier being 31.0 kJ·mol^{-1}. To sum up, R3 and R4 are identified to be the rate-determining in Path1 and Path2 together with the barriers of 54.6 and 93.8 kJ·mol^{-1}, showing the Path1 is the predominant route.

Additionally, it can be obtained that Pd_1-Ag(111) is advantageous to Pd_{ML}/Ag(111), Pd_4Ag_8/Ag(111) and Pd(111) in terms of the catalytic activity toward DMO generation by comparing the energy barriers (54.6, 116.7, 122.6 and 120.6 kJ·mol^{-1}) of the rate-controlling steps in

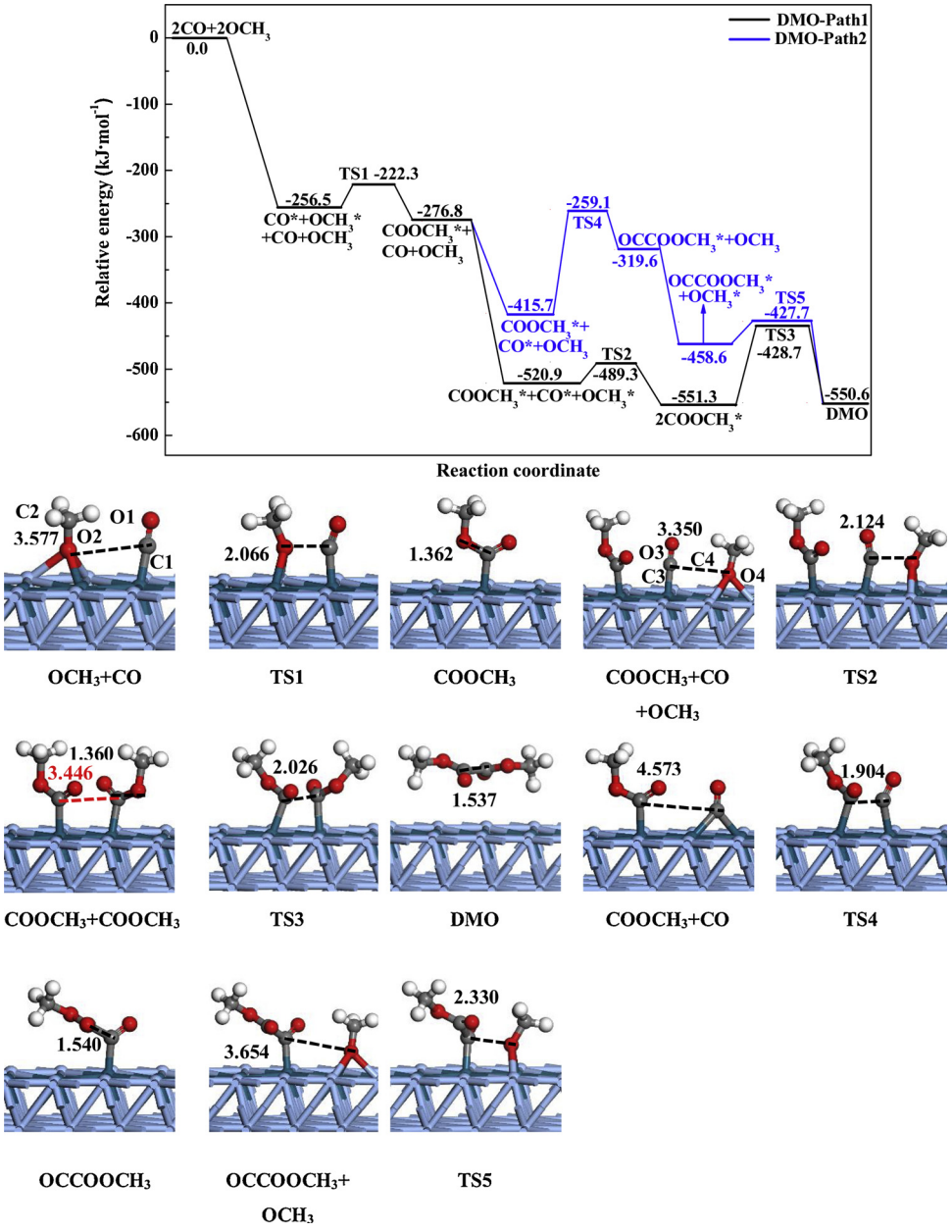

Fig. 3. The diagram of potential energy toward DMO formation together with related configurations over the Pd_4Ag_8/Ag(111).

the advantageous route, as shown in Figs. 2–4. It is because the adsorption stability of the reactive species determines the difficulty degree in its activation, where the adsorption energy of $COOCH_3$-$COOCH_3$ on Pd_1-Ag(111) is the most weakest (-281.0 kJ·mol^{-1}), compared with that (-343.8 and -337.5 kJ·mol^{-1}) on Pd_4Ag_8/Ag(111) and Pd_{ML}/Ag(111), thereby resulting in that the activation energy barrier is the lowest. Generally, when the reaction species on the catalyst possesses moderate weaker chemisorption energy, its activation energy barrier would be lower. For example, Zhang et al. [54] studied CO oxidation reaction on $Pd_{19}Au$, $Pd_{18}Au_2$, $Pd_{17}Au_3$ and $Pd_{16}Au_4$ alloy surfaces, where the adsorption energy of the reactive species of CO-O on these catalysts were -520.1, -447.7, -398.5 and -330.9 kJ·mol^{-1}, respectively. As a result, the corresponding activation barriers were 85.9, 70.4, 33.8 and 20.3 kJ·mol^{-1}, respectively. Additionally, the similar study of CO oxidation reaction on Pd and Pd-Ni-Pd catalysts also obtained that the adsorption energy of CO-O was relatively weaker (-511.4 vs -463.1 kJ·mol^{-1}), and the corresponding activation energy barrier was lower (67.5 vs 53.1 kJ·mol^{-1}) [55].

3.2. Comparison of DMO and DMC generation

Apart from the study of DMO production, the side-product dimethyl carbonate ($CH_3OCOOCH_3$, DMC) formation has also been investigated. DMC is generated via $COOCH_3$ intermediate attacking OCH_3 based on co-adsorption of $COOCH_3$, OCH_3 and CO, in which the influence of CO on DMC generation is premeditated due to redundant CO in the realistic reaction [11]. It is found that the energy barrier (59.5 kJ·mol^{-1}) of DMC formation is lower than that (116.7 kJ·mol^{-1}) of $2COOCH_3$ → DMO in advantageous pathway on the Pd_{ML}/Ag(111), which indicates that DMC synthesis is strikingly better than DMO generation, yet DMO is much more advantageous to be generated on the Pd_4Ag_8/Ag(111) and Pd_1-Ag(111) via the comparison of the activation barriers (122.6 versus 266.3, 54.6 versus 97.5) of rate-controlling step in dominate pathway of DMO and DMC formation, as presented in Fig. 5. Thus, the DMO (main product) is much more favorable to be synthesized than the DMC (side-product) over Pd_4Ag_8/Ag(111) and Pd_1-Ag(111), while it is opposite on the Pd_{ML}/Ag(111).

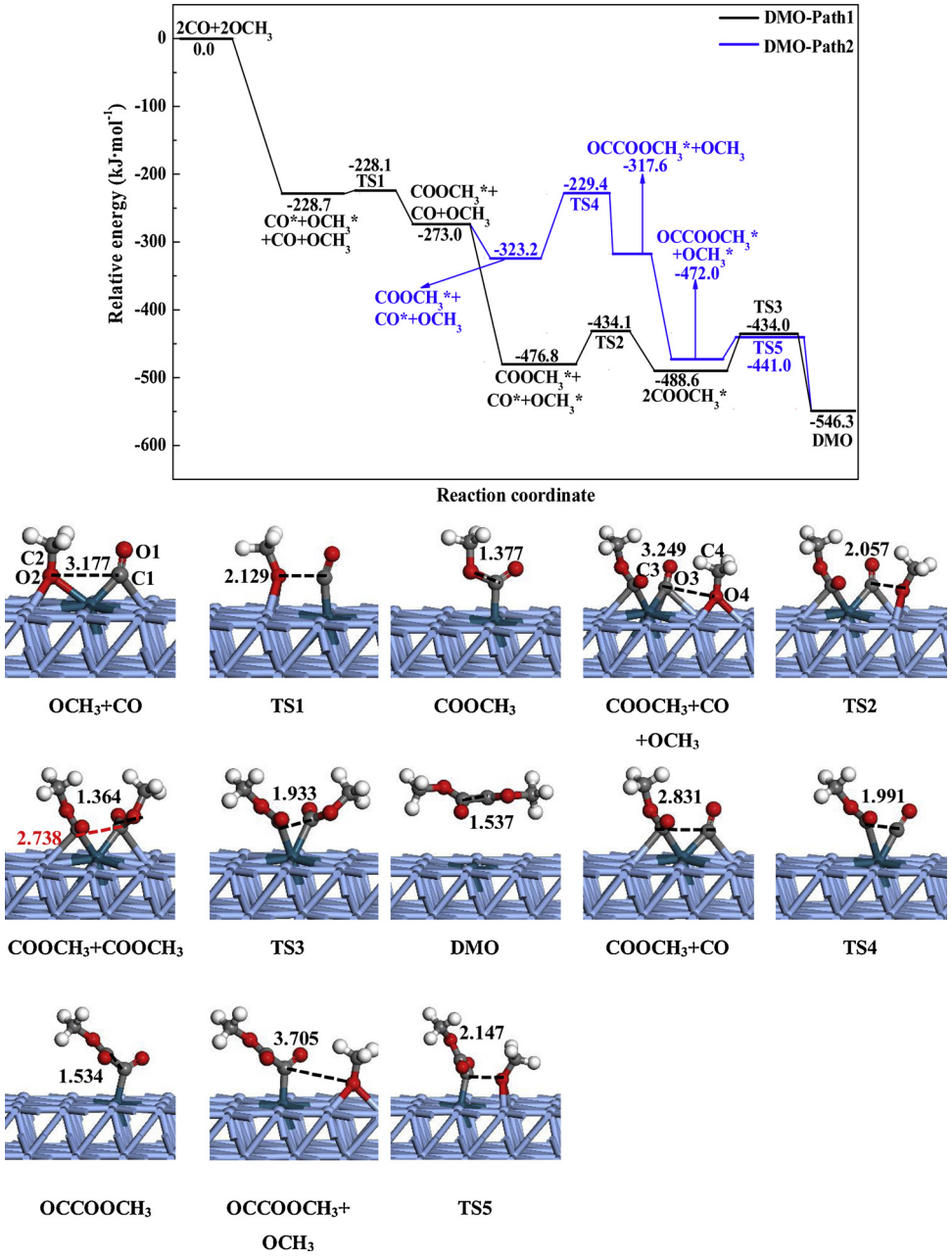

Fig. 4. The energy diagram toward DMO formation with corresponding configurations over the Pd_1-Ag(111).

As a result, Ag substrate doped by Pd stripe can improve the selectivity for DMO formation, while the activity is slightly decreased. And, Ag substrate doped by Pd single atom not only improves the selectivity for DMO formation but also greatly enhances the activity. More excitingly, the catalytic performance for DMO formation on Ag substrate doped by Pd single atom is also far superior to that on Cu substrate doped by Pd stripe or Pd single atom [7].

3.3. Micro-kinetic analysis

Based on the analysis of above energy barrier results, it can be obtained CO + CH_3O → $COOCH_3$ + (CO + OCH_3) → $2COOCH_3$ → DMO is the dominate path to synthesize DMO on these surfaces, in which $2COOCH_3$ → DMO is the rate-controlling step. In the light of activation barrier of the rate-controlling step, it can be acquired that Pd_1-Ag(111) displays the highest activity for DMO formation, Pd_{ML}/Ag(111) is slightly superior to Pd(111), while Pd_4Ag_8/Ag(111) is a little inferior to Pd(111), as presented in Fig. 6.

For the purpose of further grasp the activity and selectivity of DMO formation at the realistic condition, the micro-kinetic analysis [56–59] based on transition state theory is executed by considering the factors of temperatures and pressures (T: 375 − 415 K, P_{CO}: 280 kPa, P_{CH3ONO}: 200 kPa) in experiment [11]. Firstly, the adsorption processes of initial reactants (CO and OCH_3) are postulated to be in the state of equilibrium and the corresponding equilibrium constants (K) are obtained in light of the formulas (5), (6), which is listed in Table 3. Secondly, the coverage of species can be calculated via the formulas (7)–(11) based on steady-state approximation theory, as presented in Table 4. Lastly, the production rate of DMO and DMC can be acquired by the following expressions:

$$r_{DMO} = k_3\theta^2_{COOCH_3} + k_5\theta_{OCCOOCH_3}\theta_{OCH_3} \quad (12)$$

and

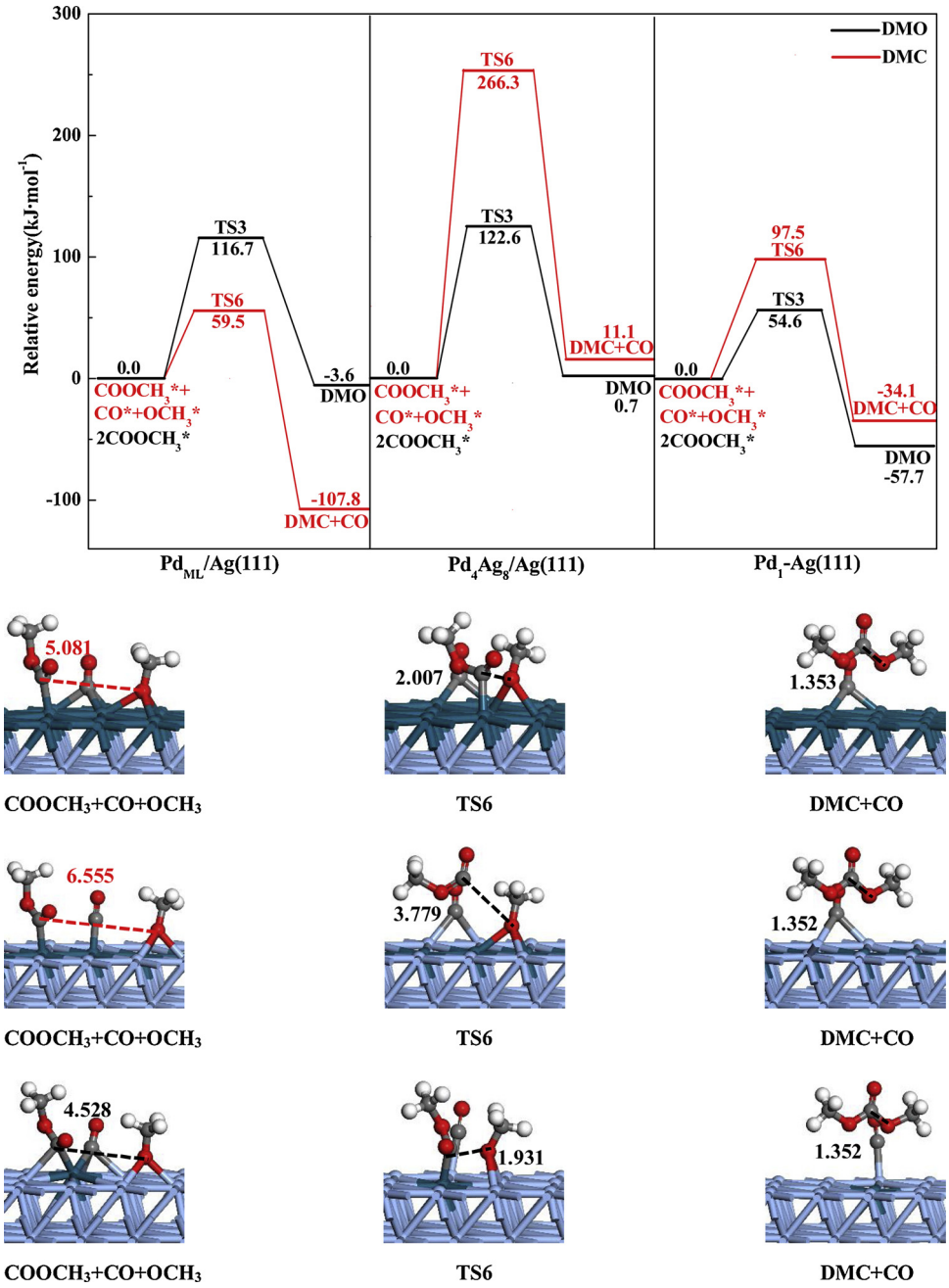

Fig. 5. The comparison of potential energy diagram toward the rate-controlling step in dominate route to generate DMO and DMC over the Pd_{ML}/Ag(111), Pd_4Ag_8/Ag(111) and Pd_1-Ag(111).

$$r_{DMC} = k_6 \theta_{COOCH_3} \theta_{OCH_3} \tag{13}$$

respectively, which is exhibited in Table 5.

$$K = \exp[-(\Delta E_{ads} - T(S_{adsorbate} - S_{gas}))/RT] \tag{5}$$

$$S = R\sum_{i=1}^{3N}\left[-\ln\left(1-\exp(-\frac{h\nu_i}{k_B T})\right) + \frac{h\nu_i}{k_B T}\frac{\exp(-\frac{h\nu_i}{k_B T})}{1-\exp(-\frac{h\nu_i}{k_B T})}\right] \tag{6}$$

where ΔE_{ads} and $S_{adsorbate}$ denote the adsorption energies and entropies of CO or OCH_3 over catalyst surfaces, additionally, S_{gas} means the gas phase entropy [60].

$$\theta_{CO} = P_{CO} K_{CO} \theta^* \tag{7}$$

$$\theta_{OCH_3} = P_{OCH_3} K_{OCH_3} \theta^* \tag{8}$$

$$\theta_{COOCH_3}: \frac{d\theta_{COOCH_3}}{dt} = k_1\theta_{OCH_3}\theta_{CO} + k_2\theta_{OCH_3}\theta_{CO} - k_3\theta^2_{COOCH_3} - k_4\theta_{COOCH_3}\theta_{CO} - k_6\theta_{COOCH_3}\theta_{OCH_3} = 0 \tag{9}$$

$$\theta_{OCCOOCH_3}: \frac{d\theta_{OCCOOCH_3}}{dt} = k_4\theta_{COOCH_3}\theta_{CO} - k_5\theta_{OCCOOCH_3}\theta_{OCH_3} = 0 \tag{10}$$

$$\theta_{CO} + \theta_{OCH_3} + \theta_{COOCH_3} + \theta_{OCCOOCH_3} + \theta^* = 1 \tag{11}$$

Among these, the coverage calculation is executed on basis of taking the coverage of entire surface being 1. On the Pd_1-Ag(111) surface, the entire surface refers to Pd single atom and other Ag atoms, and each atom (Pd or Ag) is regarded as one site. The similar micro-kinetic model has been applied to other single atom surface alloys catalytic reactions [61–64]. Zhou et al. [61] adopted density functional theory calculations and micro-kinetic model to study hydrodeoxygenation of phenol

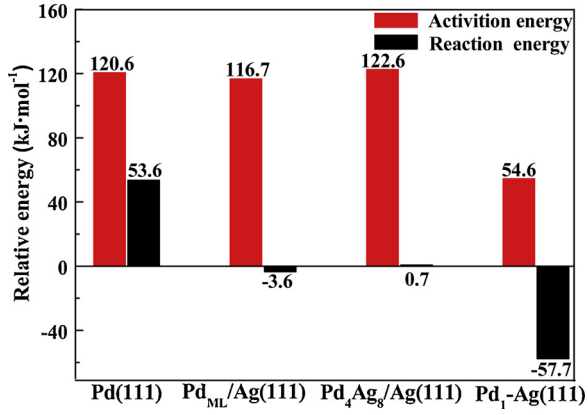

Fig. 6. The energy diagram for $2COOCH_3 \rightarrow$ DMO, the rate-controlling step of the favorable route for DMO formation.

on Ni-based bimetallic single atom surface alloys denoted as M@Ni (111) (M = Sc, Ti, V, Cr, Mn, Fe, Co, Mo, W, and Re), where phenol was adsorbed on M atom and adjacent Ni atoms, and the sum of the coverage of adsorbed species and free adsorption sites was considered to being 1 on entire surface.

In the study, it can be known that the DMO generation rate is in the order of Pd_1-Ag(111) > Pd_{ML}/Ag(111) > Pd(111) > Pd_4Ag_8/Ag(111), as presented in Table 5. Additionally, the formation rate about DMO is far-off superior to that about DMC over Pd_1-Ag(111) and Pd_4Ag_8/Ag (111), while the generation rate about DMO is smaller than that about DMC over Pd_{ML}/Ag(111). Accordingly, it is found that only Pd_1-Ag (111) surface possesses both outstanding activity and selectivity for DMO production. The similar micro-kinetic analysis was employed to obtain that activity and selectivity toward DMO production over Pd_{ML}/Cu(111), Pd_4Cu_8/Cu(111) and Pd_1-Cu(111) [7,50].

3.4. Respective role of strain and ligand effect toward catalytic activity of DMO formation

The unusual catalytic performance of bimetallic catalysts is well-known attributed to the combination of strain and ligand effect. The strain effect emerges from the tension or compression of strain originating from carrier to doped metal, as well as the ligand effect appears from the transfer of charge between carrier and doped metal [33–37]. On the Pd_1-Ag(111) surface, the strain effect refers to the tensile strain caused by doping a smaller Pd atom into a larger Ag lattice. And, the strain area on the Pd_1-Ag (111) surface only refers to around the Pd single atom, where the reaction of CO oxidative coupling to DMO is proceeded. The similar studies about strain effect on the single atom surface alloy has been reported in the previous theoretical and experimental work [65–69]. Thirumalai et al. [65] has studied the reactions of nitric oxide dissociation and acetylene hydrogenation to ethylene on Pd_1-Au and Pd_1-Ag single atom surface alloy by using density functional theory calculations, found that the activity of these catalysts was enhanced in comparison with that of pure Pd, and further obtained that it was due to the tensile strain effect caused by adding a single atom of Pd to Au and Ag surfaces.

The average bond length between Pd and neighboring atoms on the optimized Pd(111), Pd_{ML}/Ag(111), Pd_4Ag_8/Ag(111) and Pd_1-Ag(111) are measured and the values are 2.797, 2.847, 2.878 and 2.903 Å, respectively, showing that Ag carriers result in the stretch of average bond length between Pd and neighboring atoms, which is so-named strain effect, and the corresponding strain values (ξ) are 1.8 %, 2.9 % and 3.8 %, respectively. Additionally, the average charge polarization (Δσ) between surface Pd atoms with Ag carrier metal on Pd_{ML}/Ag(111), Pd_4Ag_8/Ag(111) and Pd_1-Ag(111) are acquired via Bader charge analysis, of which the values are -0.06, -0.16, and -0.20 *e*, respectively, displaying the charge transfer from Ag substrates to surface Pd, which is so-called ligand effect. But the admixture of strain and ligand eff ;ect covers the essential cause of activity change of bimetallic catalysts. Thereupon, it is indispensable to segregate strain and ligand effect in order to understand relative influence toward activity.

Considering computation efficiency, the rate-controlling step of $2COOCH_3 \rightarrow$ DMO that decides the activity of DMO generation, is selected to research the impact of strain and ligand on the activity of Pd_{ML}/Ag(111), Pd_4Ag_8/Ag(111) and Pd_1-Ag(111). In reference to former study [7,70,71], the relative effect of strain (ΔE_a^{strain}) and the ligand (ΔE_a^{ligand}) as well as combined effect ($\Delta E_a^{combined}$) can be expressed as the following formulas (14)–(16), where $E_a^{strain-M}$, E_a^{Pd} and $E_a^{Pd\text{-}M}$ mean the activation energy on strained monometallic Pd(111) surface, that on the Pd(111) surface, and that on Pd_{ML}/Ag(111), Pd_4Ag_8/Ag(111) or Pd_1-Ag(111), respectively. For example, $E_a^{strain-M}$, E_a^{Pd} and $E_a^{Pd\text{-}M}$ (115.0, 120.6 and 116.7 kJ·mol^{-1}) on the Pd_{ML}/Ag(111) are firstly acquired via DFT calculation, then ΔE_a^{strain}, ΔE_a^{ligand} and $\Delta E_a^{combined}$ (-5.6, 1.7 and -3.9 kJ·mol^{-1}) can be acquired via the formulas (14)–(16).

$$\Delta E_a^{strain} = E_a^{strain\text{-}M} - E_a^{Pd} \quad (14)$$

$$\Delta E_a^{ligand} = E_a^{Pd\text{-}M} - E_a^{strain\text{-}M} \quad (15)$$

$$\Delta E_a^{combined} = \Delta E_a^{strain} + \Delta E_a^{ligand} \quad (16)$$

As presented in Fig. 7, strain effect lessens energy barrier and ligand effect raises it on the Pd_{ML}/Ag(111), however it is reverse on the Pd_4Ag_8/Ag(111), where strain effect is superior to ligand effect, thereby leading to the activity improved on the Pd_{ML}/Ag(111) but fallen on the Pd_4Ag_8/Ag(111). Additionally, strain and ligand effect both subside the barrier on the Pd_1-Ag(111), therefore extremely enhancing the activity for DMO generation. The same means has been applied to interpret the relative role of strain and ligand effect toward activity of DMO formation on the Pd_{ML}/Cu(111), Pd_4Cu_8/Cu(111) and Pd_1-Cu(111) [7,50].

4. Conclusions

In this work, CO oxidation to DMO has been investigated over Pd_{ML}/Ag(111), Pd_4Ag_8/Ag(111) and Pd_1-Ag(111) by DFT calculation in conjunction with micro-kinetic model, so as to obtain a dilute Pd content of Pd-Ag bimetallic catalysts under the premise of maintaining the catalytic performance. The results indicate that the favorable route to DMO generation is $CO + CH_3O \rightarrow COOCH_3 + (CO + OCH_3) \rightarrow 2COOCH_3 \rightarrow$ DMO over three catalyst surfaces, where the $2COOCH_3 \rightarrow$ DMO is the rate-controlling step. The combined energy barrier and

Table 3
The adsorption equilibrium constants of CO and OCH_3.

		375 K	385 K	395 K	405 K	415 K
Pd_{ML}/Ag(111)	K_{CO}	1.95×10^{12}	7.47×10^{11}	3.00×10^{11}	1.26×10^{11}	5.52×10^{10}
	K_{OCH3}	1.92×10^{9}	8.05×10^{8}	3.53×10^{8}	1.62×10^{8}	7.68×10^{7}
Pd_4Ag_8/Ag(111)	K_{CO}	6.86×10^{9}	2.84×10^{9}	1.23×10^{9}	5.57×10^{8}	2.62×10^{8}
	K_{OCH3}	3.08×10^{16}	8.72×10^{15}	2.63×10^{15}	8.40×10^{14}	2.84×10^{14}
Pd_1-Ag(111)	K_{CO}	6.73×10^{9}	2.77×10^{9}	1.19×10^{9}	5.37×10^{8}	2.51×10^{8}
	K_{OCH3}	5.64×10^{18}	1.43×10^{18}	3.87×10^{17}	1.12×10^{17}	3.44×10^{16}

Table 4
The surface coverage for each species.

		375 K	385 K	395 K	405 K	415 K
Pd_{ML}/Ag(111)	θ^*	7.13×10^{-20}	2.23×10^{-19}	6.60×10^{-19}	1.85×10^{-18}	4.91×10^{-18}
	θ_{CO}	3.83×10^{-5}	5.04×10^{-5}	6.53×10^{-5}	8.36×10^{-5}	1.06×10^{-4}
	θ_{OCH3}	2.79×10^{-2}	3.34×10^{-2}	3.96×10^{-2}	4.65×10^{-2}	5.42×10^{-2}
	θ_{COOCH3}	9.72×10^{-1}	9.67×10^{-1}	9.60×10^{-1}	9.53×10^{-1}	9.46×10^{-1}
	$\theta_{OCCOOCH3}$	1.80×10^{-18}	4.55×10^{-18}	1.10×10^{-17}	2.54×10^{-17}	5.65×10^{-17}
Pd_4Ag_8/Ag(111)	θ^*	2.08×10^{-26}	8.70×10^{-26}	3.38×10^{-25}	1.23×10^{-24}	4.20×10^{-24}
	θ_{CO}	3.99×10^{-11}	6.93×10^{-11}	1.17×10^{-10}	1.92×10^{-10}	3.07×10^{-10}
	θ_{OCH3}	1.28×10^{-4}	1.52×10^{-4}	1.78×10^{-4}	2.07×10^{-4}	2.38×10^{-4}
	θ_{COOCH3}	1.00×10^{0}	1.00×10^{0}	1.00×10^{0}	1.00×10^{0}	1.00×10^{0}
	$\theta_{OCCOOCH3}$	3.12×10^{-24}	1.32×10^{-23}	5.16×10^{-23}	1.90×10^{-22}	6.54×10^{-22}
Pd_1-Ag(111)	θ^*	7.37×10^{-25}	2.90×10^{-24}	1.07×10^{-23}	3.68×10^{-23}	1.19×10^{-22}
	θ_{CO}	1.39×10^{-9}	2.25×10^{-9}	3.57×10^{-9}	5.53×10^{-9}	8.38×10^{-9}
	θ_{OCH3}	8.31×10^{-1}	8.28×10^{-1}	8.26×10^{-1}	8.23×10^{-1}	8.21×10^{-1}
	θ_{COOCH3}	1.69×10^{-1}	1.72×10^{-1}	1.74×10^{-1}	1.77×10^{-1}	1.79×10^{-1}
	$\theta_{OCCOOCH3}$	2.92×10^{-16}	8.35×10^{-16}	2.26×10^{-15}	5.84×10^{-15}	1.44×10^{-14}

Table 5
The rates (s^{-1}·$site^{-1}$) of DMO and DMC generation.

		375 K	385 K	395 K	405 K	415 K
Pd_{ML}/Ag(111)	DMO	5.20×10^{-5}	1.37×10^{-4}	3.43×10^{-4}	8.20×10^{-4}	1.87×10^{-3}
	DMC	5.72×10^{0}	6.14×10^{0}	6.54×10^{0}	6.91×10^{0}	7.27×10^{0}
Pd_4Ag_8/Ag(111)	DMO	6.50×10^{-7}	1.74×10^{-6}	4.43×10^{-6}	1.08×10^{-5}	2.50×10^{-5}
	DMC	8.52×10^{-27}	9.64×10^{-26}	9.64×10^{-25}	8.61×10^{-24}	6.91×10^{-23}
Pd_1-Ag(111)	DMO	8.11×10^{3}	1.33×10^{4}	2.13×10^{4}	3.34×10^{4}	5.11×10^{4}
	DMC	3.43×10^{-2}	7.98×10^{-2}	1.78×10^{-1}	3.80×10^{-1}	7.85×10^{-1}
Pd(111)[a]	DMO	4.72×10^{-6}	1.29×10^{-5}	3.35×10^{-5}	5.31×10^{-5}	1.98×10^{-4}
	DMC	4.02×10^{-14}	2.45×10^{-13}	1.11×10^{-12}	4.02×10^{-12}	6.04×10^{-12}

[a] The study in Ref [50].

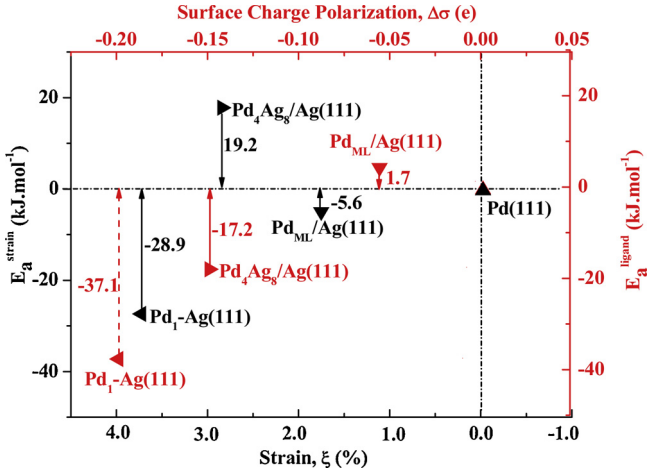

Fig. 7. The relative effect of strain and ligand toward the rate-controlling step, $2COOCH_3 \rightarrow$ DMO.

micro-kinetic results display the activity toward DMO generation is in order of Pd_1-Ag(111) > Pd_{ML}/Ag(111) > Pd(111) > Pd_4Ag_8/Ag(111). Additionally, the influence of strain and ligand on activity of Pd-Ag bimetallic catalysts has also been probed into, it is found that strain effect lowers energy barrier and ligand effect enhances it on the Pd_{ML}/Ag(111), while it is opposite on the Pd_4Ag_8/Ag(111), where strain effect is prevail than ligand effect, thereby resulting in the activity increased on the Pd_{ML}/Ag(111) while decreased on the Pd_4Ag_8/Ag(111). On the Pd_1-Ag(111), strain and ligand effect both reduce barrier, thus significantly increasing the activity toward DMO formation. And, the high DMO selectivity appears on the Pd_1-Ag(111), whereas the opposite phenomenon happens on the Pd_{ML}/Ag(111). Therefore, it is suggested to attempt the Pd_1-Ag single atom surface alloy experimentally to enhance the catalytic performance toward DMO synthesis and whittle down the expense.

CRediT authorship contribution statement

Bingying Han: Conceptualization, Data curation, Formal analysis, Validation, Writing - original draft. **Lixia Ling:** Conceptualization, Data curation, Formal analysis, Funding acquisition, Investigation, Methodology, Project administration, Resources, Software, Validation, Writing - review & editing. **Riguang Zhang:** Supervision, Funding acquisition. **Ping Liu:** Writing - review & editing. **Maohong Fan:** Writing - review & editing. **Baojun Wang:** Investigation, Methodology, Software, Supervision, Writing - review & editing, Funding acquisition.

Declaration of Competing Interest

The authors declare that they have no known competing financial interests or personal relationships that could have appeared to influence the work reported in this paper.

Acknowledgments

We gratefully acknowledge financial support from the Key Projects of National Natural Science Foundation of China (21736007), the National Natural Science Foundation of China (Grant Nos. 21576178 and 21476155), Research Project Supported by Shanxi Scholarship Council of China (No. 2016-030) and the Foundation of State Key Laboratory of Coal Conversion (No. J18-19-602)

References

[1] J. Ding, Y.T. Liu, J. Zhang, M. Dong, Y.X. Wang, W.X. He, X.X. Han, K.F. Liu, Z. Jiang, J.G. Chen, Synergism from interfaces between Cu and crystalline ZrO_2 nanosheets fabricated by acetic complex method for oxalates hydrogenation, Mol. Catal. 438 (2017) 93–102.
[2] G.Q. Cui, X.Y. Meng, X. Zhang, W.L. Wang, S.L. Xu, Y.C. Ye, K.J. Tang, W.M. Wang,

J.H. Zhu, M. Wei, D.G. Evans, X. Duan, Low-temperature hydrogenation of dimethyl oxalate to ethylene glycol via ternary synergistic catalysis of Cu and acid-base sites, Appl. Catal. B: Environ. 248 (2019) 394–404.
[3] R.P. Ye, L. Lin, C.C. Chen, J.X. Yang, F. Li, X. Zhang, D.J. Li, Y.Y. Qin, Z.F. Zhou, Y.G. Yao, Synthesis of robust MOF-derived Cu/SiO_2 catalyst with low copper loading via sol-gel method for the dimethyl oxalate hydrogenation reaction, ACS Catal. 8 (2018) 3382–3394.
[4] D.M. Fenton, P.J. Steinwand, Noble metal catalysis. III. Preparation of dialkyl oxalates by oxidative carbonylation, J. Org. Chem. 39 (1974) 701–704.
[5] N. Saliba, J. Wang, B.A. Bansenauer, B.E. Koel, Adsorption and reaction of nitromethane (CH_3NO_2) on Pt(111), Surf. Sci. 389 (1997) 147–161.
[6] C. Fan, M. Luo, W.D. Xiao, Reaction mechanism of methyl nitrite dissociation during CO catalytic coupling to dimethyl oxalate: a density functional theory study, Chin. J. Chem. Eng. 24 (2016) 132–139.
[7] B.Y. Han, L.X. Ling, M.H. Fan, P. Liu, B.J. Wang, R.G. Zhang, A DFT study and microkinetic analysis of CO oxidation to dimethyl oxalate over Pd stripe and Pd single atom-doped Cu(111) surfaces, Appl. Surf. Sci. 479 (2019) 1057–1067.
[8] Q.H. Li, Z.F. Zhou, R.P. Chen, B.Z. Sun, L.Y. Qiao, Y.G. Yao, K.C. Wu, Insights into the reaction mechanism of CO oxidative coupling to dimethyl oxalate over palladium: a combined DFT and IR study, Phys. Chem. Chem. Phys. 17 (2015) 9126–9134.
[9] C.Z. Wang, P.J. Chen, Y.K. Li, G.F. Zhao, Y. Liu, Y. Lu, In situ DRIFTS study of CO coupling to dimethyl oxalate over structured Al-fiber@ns-AlOOH@Pd catalyst, J. Catal. 344 (2016) 173–183.
[10] C.Z. Wang, W.S. Xu, Z.X. Qin, S. Mintova, Spontaneous galvanic deposition of nanoporous Pd on microfibrous-structured Al-fibers for CO oxidative coupling to dimethyl oxalate, Catal. Commun. 119 (2019) 39–41.
[11] Z.N. Xu, J. Sun, C.S. Lin, X.M. Jiang, Q.S. Chen, S.Y. Peng, M.S. Wang, G.C. Guo, High-performance and long-lived Pd nanocatalyst directed by shape eff ;ect for CO oxidative coupling to dimethyl oxalate, ACS Catal. 3 (2013) 118–122.
[12] S.Y. Peng, Z.N. Xu, Q.S. Chen, Y.M. Chen, J. Sun, Z.Q. Wang, M.S. Wang, G.C. Guo, An ultra-low Pd loading nanocatalyst with high activity and stability for CO oxidative coupling to dimethyl oxalate, Chem. Commun. 49 (2013) 5718–5720.
[13] R.G. Zhang, Y. Wang, B.J. Wang, L.X. Ling, Probing into the effects of cluster size and Pd ensemble as active center on the activity of H_2 dissociation over the noble metal Pd-doped Cu bimetallic clusters, Mol. Catal. 475 (2019) 110457-1-10.
[14] Y. Cheng, H. Pham, J.J. Huo, R. Johnson, A.K. Datye, B. Shanks, High activity Pd-Fe bimetallic catalysts for aqueous phase hydrogenations, Mol. Catal. 477 (2019) 110546-1-8.
[15] M. Pudukudy, Z. Yaakob, Z.S. Akmal, Direct decomposition of methane over Pd promoted Ni/SBA-15 catalysts, Appl. Surf. Sci. 353 (2015) 127–136.
[16] P. Castaño, B. Pawelec, J.L.G. Fierro, J.M. Arandes, J. Bilbao, Enhancement of pyrolysis gasoline hydrogenation over Pd-promoted Ni/SiO_2–Al_2O_3 catalysts, Fuel 86 (2007) 2262–2274.
[17] Y.P. Li, S.M. Chen, R. Long, H.X. Ju, Z.W. Wang, X.X. Yu, F.Y. Gao, Z.J. Cai, C.M. Wang, Q. Xu, J. Jiang, J.F. Zhu, L. Song, Y.J. Xiong, Near-surface dilution of trace Pd atoms to facilitate Pd-H bond cleavage for giant enhancement of electrocatalytic hydrogen evolution, Nano Energy 34 (2017) 306–312.
[18] J.S. Wang, C.H. Liu, A. Lushington, N.C. Cheng, M.N. Banis, A. Riese, X.L. Sun, Pd on carbon nanotubes-supported Ag for formate oxidation: the effect of Ag on anti-poisoning performance, Electrochim. Acta 210 (2016) 285–292.
[19] J. Cho, S. Lee, J. Han, S.P. Yoon, S.W. Nam, S.H. Choi, K.Y. Lee, H.C. Ham, Importance of ligand effect in selective hydrogen formation via formic acid decomposition on the bimetallic Pd/Ag catalyst from first-principles, J. Phys. Chem. C. 118 (2014) 22553–22560.
[20] G.C. Smith, C. Norris, C. Binns, H.A. Padmore, A photoemission study of ultra-thin palladium overlayers on low-index faces of silver, J. Phys. C: Solid State Phys. 15 (1982) 6481–6496.
[21] J.P. Muscat, Chemisorption properties of thin Pd overlayers on Nb(110) and Ag (111), Surf. Sci. 131 (1983) 299–308.
[22] G.C. Smith, C. Norris, C. Binns, The electron states of ultra-thin Pd overlayers on Cu (100) and Ag(111), Vacuum 31 (1981) 523–524.
[23] K. Häupl, P. Wiβmann, X-ray diffraction studies on thin palladium films epitaxially grown on Ag(111), Thin Solid Films 174 (1989) 105–109.
[24] K. Tedsree, T. Li, S. Jones, C.W.A. Chan, K.M.K. Yu, P.A.J. Bagot, E.A. Marquis, G.D.W. Smith, S.C.E. Tsang, Hydrogen production from formic acid decomposition at room temperature using a Ag-Pd core-shell nanocatalyst, Nat. Nanotechnol. 6 (2011) 302–307.
[25] S. Jaatinen, P. Salo, M. Alatalo, K. Kokko, Effect of the electronic structure on CO oxidation on Pd doped Ag(111), Surf. Sci. 566 (2004) 1063–1066.
[26] R. Ma, Y.F. He, J.T. Feng, Z.Y. Hu, G.V. Tendeloo, D.Q. Li, A facile synthesis of Ag@PdAg core-shell architecture for efficient purification of ethene feedstock, J. Catal. 369 (2019) 440–449.
[27] P. Aich, H.J. Wei, B. Basan, A.J. Kropf, N.M. Schweitzer, C.L. Marshall, J.T. Miller, R. Meyer, Single-atom alloy Pd − Ag catalyst for selective hydrogenation of acrolein, J. Phys. Chem. C 119 (2015) 18140–18148.
[28] H. Chen, Q.H. Lu, C.H. Yi, B.L. Yang, S.T. Qi, Design of bimetallic Rh-M catalysts for N_2O decomposition: from DFT calculation to experimental study, Mol. Catal. 446 (2018) 1–9.
[29] M.H. Zhang, H. Gong, Y.Z. Yu, DFT study of key elementary steps for C_2^+ alcohol synthesis on bimetallic sites of Cu-Co shell-core structure from syngas, Mol. Catal. 443 (2017) 165–174.
[30] J.T. Niu, J.Y. Ran, X.S. Du, W.J. Qi, P. Zhang, L. Yang, Effect of Pt addition on resistance to carbon formation of Ni catalysts in methane dehydrogenation over Ni-Pt bimetallic surfaces: a density functional theory study, Mol. Catal. 434 (2017) 206–218.
[31] A. Estejab, G.G. Botte, Ammonia oxidation kinetics on bimetallic clusters of platinum and iridium: a theoretical approach, Mol. Catal. 445 (2018) 279–292.
[32] F. Jalid, T.S. Khan, F.Q. Mir, M.A. Haider, Understanding trends in hydrodeoxygenation reactivity of metal and bimetallic alloy catalysts from ethanol reaction on stepped surface, J. Catal. 353 (2017) 265–273.
[33] T. Ishihara, S. Fang, T. Ide, Effects of strain induced by Au dispersion in Ba and Ni doped Y_2O_3 on direct decomposition of NO, Mol. Catal. 475 (2019) 110488-1-7.
[34] T.A. Maark, B.R.K. Nanda, Enhancing CO_2 electroreduction by tailoring strain and ligand effects in bimetallic copper-rhodium and copper-nickel heterostructures, J. Phys. Chem. C 121 (2017) 4496–4504.
[35] F.Z. Liu, C. Wu, S.C. Yang, Strain and ligand effects on CO_2 reduction reactions over Cu-metal heterostructure catalysts, J. Phys. Chem. C 121 (2017) 22139–22146.
[36] B.S. Choi, J. Song, M.J. Song, B.S. Goo, Y.W. Lee, Y. Kim, H. Yang, S.W. Han, Core-shell engineering of Pd-Ag bimetallic catalysts for efficient hydrogen production from formic acid decomposition, ACS Catal. 9 (2019) 819–826.
[37] J.R. Kitchin, J.K. Nørskov, M.A. Barteau, J.G. Chen, Role of strain and ligand eff ;ects in the modification of the electronic and chemical properties of bimetallic surfaces, Phys. Rev. Lett. 93 (2004) 156801-1-4.
[38] G. Kresse, J. Hafner, Ab initio molecular-dynamics simulation of the liquid-metal amorphous-semiconductor transition in germanium, Phys. Rev. B: Condens. Matter Mater. Phys. 49 (1994) 14251–14269.
[39] G. Kresse, J. Furthmüller, Efficiency of ab-initio total energy calculations for metals and semiconductors using a plane-wave basis set, Comput. Mater. Sci. 6 (1996) 15–50.
[40] M. Ernzerhof, J.P. Perdew, Generalized gradient approximation to the angle- and system-averaged exchange hole, Phys. Rev. Lett. 109 (1998) 3313–3320.
[41] J.J. Mortensen, L.B. Hansen, K.W. Jacobsen, Real-space grid implementation of the projector augmented wave method, Phys. Rev. B: Condens. Matter Mater. Phys. 71 (2005) 035109-1-11.
[42] P.E. Blöchl, O. Jepsen, O.K. Andersen, Improved tetrahedron method for Brillouin-zone integrations, Phys. Rev. B: Condens. Matter Mater. Phys. 49 (1994) 16223–16233.
[43] G. Henkelman, H. Jónsson, Improved tangent estimate in the nudged elastic band method for finding minimum energy paths and saddle points, J. Chem. Phys. 113 (2000) 9978–9985.
[44] G. Henkelman, B.P. Uberuaga, H. Jónsson, A climbing image nudged elastic band method for finding saddle points and minimum energy paths, J. Chem. Phys. 113 (2000) 9901–9904.
[45] P.H. Xiao, D. Sheppard, J. Rogal, G. Henkelman, Solid-state dimer method for calculating solid-solid phase transitions, J. Chem. Phys. 140 (2014) 174104-1-6.
[46] G. Henkelman, H. Jónsson, A dimer method for finding saddle points on high dimensional potential surfaces using only first derivatives, J. Chem. Phys. 111 (1999) 7010–7022.
[47] J.P. Clay, J.P. Greeley, F.H. Ribeiro, W.N. Delgass, W.F. Schneider, DFT comparison of intrinsic WGS kinetics over Pd and Pt, J. Catal. 320 (2014) 106–117.
[48] J. Häglund, A.F. Guillermet, G. Grimvall, M. Körling, Theory of bonding in transition-metal carbides and nitrides, Phys. Rev. B: Condens. Matter Mater. Phys. 48 (1993) 11685–11691.
[49] I.K. Suh, H. Ohta, Y. Waseda, High-temperature thermal expansion of six metallic elements measured by dilatation method and X-ray diffraction, J. Mater. Sci. 23 (1988) 757–760.
[50] B.Y. Han, X. Feng, L.X. Ling, M.H. Fan, P. Liu, R.G. Zhang, B.J. Wang, CO oxidative coupling to dimethyl oxalate over Pd-Me (Me = Cu, Al) catalysts: a combined DFT and kinetic study, Phys. Chem. Chem. Phys. 20 (2018) 7317–7332.
[51] D. Jiang, S. Dai, The role of low-coordinate oxygen on Co_3O_4(110) in catalytic CO oxidation, Phys. Chem. Chem. Phys. 13 (2011) 978–984.
[52] Y.T. Cao, L.X. Ling, H. Lin, M.H. Fan, P. Liu, R.G. Zhang, B.J. Wang, DFT study on CO oxidative coupling to DMO over Pd_4/TiO_2 and Pd_4/TiO_2-Ov: a role of oxygen vacancy on support, Comp. Mater. Sci. 159 (2019) 1–11.
[53] R.G. Zhang, M. Peng, T. Duan, B.J. Wang, Insight into size dependence of C2 oxygenate synthesis from syngas on Cu cluster: the effect of cluster size on the selectivity, Appl. Surf. Sci. 407 (2017) 282–296.
[54] J. Zhang, H.M. Jin, M.B. Sullivan, F.C.H. Lim, P. Wu, Study of Pd–Au bimetallic catalysts for CO oxidation reaction by DFT calculations, Phys. Chem. Chem. Phys. 11 (2009) 1441–1446.
[55] F.C.H. Lim, J. Zhang, H.M. Jin, M.B. Sullivan, P. Wu, A density functional theory study of CO oxidation on Pd-Ni alloy with sandwich structure, Appl. Catal. A: Gen. 451 (2013) 79–85.
[56] B.Y. Han, H. Lin, L.X. Ling, P. Liu, M.H. Fan, B.J. Wang, R.G. Zhang, A DFT study on dimethyl oxalate synthesis over Pd_{ML}/Ni(111) and Pd_{ML}/Co(111) surfaces, Appl. Surf. Sci. 465 (2019) 498–508.
[57] A. Asiaee, K.M. Benjamin, A density functional theory based elementary reaction mechanism for early steps of Fischer-Tropsch synthesis over cobalt catalyst. 2. Microkinetic modeling of liquid-phase vs. gaseous-phase process, Mol. Catal. 436 (2017) 210–217.
[58] M.H. Hansen, J.K. Nørskov, T. Bligaard, First principles micro-kinetic model of catalytic non-oxidative dehydrogenation of ethane over close-packed metallic facets, J. Catal. 374 (2019) 161–170.
[59] Y.M. Choi, P. Liu, Mechanism of ethanol synthesis from syngas on Rh(111), J. Am. Chem. Soc. 131 (2009) 13054–13061.
[60] X.M. Cao, R. Burch, C. Hardacre, P. Hu, An understanding of chemoselective hydrogenation on crotonaldehyde over Pt(111) in the free energy landscape: the microkinetics study based on first-principles calculations, Catal. Today 165 (2011) 71–79.
[61] J.W. Zhou, W. An, Z.M. Wang, X. Jia, Hydrodeoxygenation of phenol over Ni-based bimetallic single-atom surface alloys: mechanism, kinetics and descriptor, Catal.

Sci. Tech. 9 (2019) 4314–4326.
[62] H.X. Xu, C.Q. Xu, D.J. Cheng, J. Li, Identification of activity trends for CO oxidation on supported transition-metal single atom catalysts, Catal. Sci. Tech. 7 (2017) 5860–5871.
[63] X.Y. Guo, S.G. Liu, S.P. Huang, Single Ru atom supported on defective graphene for water splitting: DFT and microkinetic investigation, Int. J. Hydrogen Energy 43 (2018) 4880–4892.
[64] H. Wen, L.Y. Huai, X. Jin, J.Y. Liu, Mechanism of nitric oxide reduction by hydrogen on Ni(110) and Ir/Ni(110): first principles and microkinetic modeling, J. Phys. Chem. C 123 (2019) 4825–4836.
[65] H. Thirumalai, J.R. Kitchin, Investigating the reactivity of single atom alloys using density functional theory, Top. Catal. 61 (2018) 462–474.
[66] F.R. Lucci, M.D. Marcinkowski, T.J. Lawton, E.C.H. Sykes, H2 activation and spillover on catalytically relevant Pt–Cu single atom alloys, J. Phys. Chem. C 119 (2015) 24351–24357.
[67] M.B. Boucher, B. Zugic, G. Cladaras, J. Kammert, M.D. Marcinkowski, T.J. Lawton, E.C.H. Sykes, M. Flytzani-Stephanopoulos, Single atom alloy surface analogs in Pd0.18Cu15 nanoparticles for selective hydrogenation reactions, Phys. Chem. Chem. Phys. 15 (2013) 12187–12196.
[68] J.P. Simonovis, A. Hunt, R.M. Palomino, S.D. Senanayake, I. Waluyo, Enhanced stability of Pt-Cu single-atom alloy catalysts: in situ characterization of the Pt/Cu (111) surface in an ambient pressure of CO, J. Phys. Chem. C 122 (2018) 4488–4495.
[69] Z.T. Wang, M.T. Darby, A.J. Therrien, M. El-Soda, A. Michaelides, M. Stamatakis, E.C.H. Sykes, Preparation, structure, and surface chemistry of Ni-Au single atom alloys, J. Phys. Chem. C 120 (2016) 13574–13580.
[70] J. Cho, S. Lee, S.P. Yoon, J. Han, S.W. Nam, K.Y. Lee, H.C. Ham, Role of heteronuclear interactions in selective H_2 formation from HCOOH decomposition on bimetallic Pd/M (M = Late Transition FCC Metal) catalysts, ACS Catal. 7 (2017) 2553–2562.
[71] F. He, K. Li, G.U. Xie, Y. Wang, M.G. Jiao, H. Tang, Z.J. Wu, Understanding the enhanced catalytic activity of Cu1@Pd3(111) in formic acid dissociation, a theoretical perspective, J. Power Sources 316 (2016) 8–16.